Received: 2 October 2023 | Revised: 1 December 2023 | Accepted: 20 December 2023

DOI: 10.1111/ijag.16654

INTERNATIONAL JOURNAL OF Applied Glass SCIENCE

SPECIAL ISSUE ARTICLE

# Impact of impurities on the thermal properties of a $Li_2S$–$SiS_2$–$LiPO_3$ glass

**Jacob Wheaton** | **Steve W. Martin**

Department of Materials Science and Engineering, Iowa State University of Science and Technology, Ames, Iowa, USA

**Correspondence**
Steve W. Martin, Department of Materials Science and Engineering, Iowa State University of Science and Technology, 528 Bissell Rd, Ames, IA 50012, USA.
Email: swmartin@iastate.edu

**Funding information**
Vehicle Technologies Office of the EERE Program of the Department of Energy, Grant/Award Number: DE-EE0008852; NASA EPSCoR Program, Grant/Award Number: 80NNSSC20M0219; Department of Energy, Battelle Memorial Institute, Pacific Northwest Division, Grant/Award Number: 679315

**Abstract**

The preparation of 0.58 $Li_2S$ + 0.315 $SiS_2$ + 0.105 $LiPO_3$ glass, and the impacts of polysulfide and $P^{1P}$ defect structure impurities on the glass transition temperature ($T_g$), crystallization temperature ($T_c$), working range ($\Delta T \equiv T_c - T_g$), fragility index, and the Raman spectra were evaluated using statistical analysis. In this study, 33 samples of this glass composition were synthesized through melt-quenching. Thermal analysis was conducted to determine the glass transition temperature, crystallization temperature, working range, and fragility index through differential scanning calorimetry. The quantity of the impurities described above was determined through Raman spectroscopy peak analysis. Elemental sulfur was doped into a glass to quantify the wt% sulfur content in the glasses. Linear regression analysis was conducted to determine the impact of polysulfide impurities and $P^{1P}$ defect impurities on the thermal properties. Polysulfide impurities were found to decrease the $T_g$ at rate of nearly 12°C per 1 wt% increase in sulfur concentration. The sulfur concentration does not have a statistically significant impact on the other properties ($\alpha = 0.05$). The $P^{1P}$ defect structure appears to decrease the resistance to crystallization of the glass by measurably decreasing the working range of the glasses, but further study is necessary to fully quantify and determine this.

**KEYWORDS**
glass transition, solid-state electrolytes, sulfide glass, sulfur

## 1 | INTRODUCTION

Solid-state electrolytes (SSEs) are of growing interest due to the proliferation of lithium-ion batteries (LIBs) in consumer electronics and electric vehicles.[1,2] Current LIB technology utilizes flammable organic liquid electrolytes, which prevent the use of high energy density lithium metal anodes due to dendrite formation and/or thermal runaway leading to combustion of the organic solvent.[3,4] SSEs present several advantages over liquid electrolytes due to their lower flammability, increased resistances to dendrite formation, and thermal degradation.[5,6]

Several classes of SSEs exist, with two of the most general classifications being polymeric and inorganic SSEs.[7,8] Inorganic SSEs typically exhibit better resistance to dendrite formation, near unity $Li^+$ transference numbers, and better thermal stability over polymeric SSEs.[9–11] Oxides and sulfides are two of the most common broad

categories of inorganic SSEs.[12,13] Oxide SSEs, such as LLZO[14–16] and LLTO,[17–20] exhibit more atmospheric and electrochemical stability, while sulfide SSEs, such as LGPS and sulfide glassy solid electrolytes (GSEs), possess higher ionic conductivities and easier processability at lower temperatures.[7,21–24]

Many of the materials being studied for use as SSEs are crystalline ceramics, but amorphous materials, especially melt quenched glasses, have a few advantages over crystalline SSEs due to their lack of grain boundaries, tunable chemistries, and ease of low-temperature melt processing.[25–27] As such, many studies have been conducted on GSEs to characterize their electrochemical and thermal properties to generate thin, highly conductive SSEs.[28,29] Many of the GSEs studied in literature are sulfide-based due to the higher ionic conductivity that the sulfide anion enables due its larger size, lower localized charge density, and higher polarizability.[30] Commonly studied sulfide GSEs include $Li_2S + P_2S_5$ or $Li_2S + SiS_2$ due to their ease of preparation and high ionic conductivities.[25,31,32]

However, these GSEs often possess impurities, seen through Raman spectroscopy, such as polysulfides, $^{-}S\text{-}(S_n)\text{-}S^{-}$, which have an intense Raman peak located at 473 $cm^{-1}$ and the $P^{1P}$ defect structure, $^{2-}S_2(S)P\text{-}P(S)S_2{}^{2-}$, in thiophosphate glasses which has measurable peak located at 390 $cm^{-1}$.[31,33,34] Sometimes, these peaks are seen in the Raman spectra without being identified in the literature as they are often at very low concentration, typically less than a few atomic percent. For these reasons, these impurities are either overlooked or simply ignored.

While these structures have been reported in both lithium and sodium ion conducting thiophosphate GSEs,[35–37] the effects of polysulfide impurities and the $P^{1P}$ structure on thermal and electrochemical properties have not been carefully examined. When reported in literature, these structures are often just mentioned in the structural analysis, with minimal discussion regarding the impact of these impurities on the properties of the glass. However, these polysulfide impurities may lead to detrimental electrochemical behavior due to the possibility of sulfur redox reactions with a lithium metal anode in a solid-state battery. As such, it is important to minimize the quantity and understand the effect of these impurities on the properties of the GSE. Here, we present the first in-depth investigation on the impact of polysulfide impurities and the $P^{1P}$ defect structure on thermal properties.

In this work, we synthesized 33 samples of a single mixed oxy-sulfide glass composition using nominally the same procedure and materials for each sample. The glass composition chosen for this study was 0.58 $Li_2S$ + 0.315 $SiS_2$ + 0.105 $LiPO_3$ due to its high ionic conductivity, good electrochemical stability, and moderate resistance to crystallization. Each sample was characterized using Raman spectroscopy to determine the quantity of polysulfide impurities and the $P^{1P}$ defect structure. The glass transition temperature, crystallization temperature, and fragility index were explored using differential scanning calorimetry (DSC). Statistical relationships between these thermal properties and impurities were explored through simple linear regression. Out of this work, we find that polysulfide impurities function as "plasticizers" in the glassy network by lowering the glass transition temperature, while the $P^{1P}$ defect structure appears to increase the rate of crystallization of a glass.

## 2 | EXPERIMENTAL

### 2.1 | Preparation of glasses

Samples of 0.58 $Li_2S$ + 0.315 $SiS_2$ + 0.105 $LiPO_3$ GSEs were prepared in an inert $N_2$ glovebox containing <5 ppm $H_2O$ and <5 ppm $O_2$. $Li_2S$ (99.9%, Alfa Aesar) was heat-treated at 900°C for 15 min in a vitreous carbon crucible prior to batching to remove potential contaminants. $SiS_2$ was also heat-treated following the same procedure, after being synthesized in-house from elemental Si (99.99%, Alfa Aesar) and sulfur (99.9995%, Alfa Aesar) following a procedure previously described.[33] Glassy $LiPO_3$ was also synthesized in-house from lithium carbonate ($Li_2CO_3$, 99%, Acros Organics) and diammonium phosphate ($(NH_4)_2HPO_4$, 99%, Acros Organics) as previously reported.[38] Samples were synthesized in 10 g batches from stoichiometric amounts of the precursors. Precursor powders were milled inside a stainless-steel mill pot using a single stainless steel milling ball in a Spex 8000 M Mixer/Mill at 1725 rpm for 7 min to obtain a homogenous well-mixed powder prior to melting. The samples were then melted for 8 min inside a vitreous carbon crucible and then poured on a brass plate and splat quenched with a second brass plate at room temperature. Some samples were melted twice, with the first melt used to determine a mass loss during melting, prior to the second melt quenching. Mass loss on melting was typically approximately 0.5 wt% and ranged from 0.15 to 1.4 wt%. Samples were stored as bulk glass shards inside the $N_2$ glovebox and labeled with a number indicating the chronological order in which they were synthesized.

### 2.2 | Differential scanning calorimetry

A total of 3–20 mg of glass was sealed into a TA instruments TZero hermetic pan inside the glove box for DSC measurements using a TA Discovery 2500 DSC equipped with an autosampler. Two different pans were packed for each sample, the first being a survey scan, where an estimate of the glass transition temperature ($T_g$) and the

crystallization temperature ($T_c$) were determined through the onset method. The survey scan followed a heating profile from 100 to 450°C at a heating rate of 20°C/min. A second DSC pan was packed and ran to determine the $T_g$ and the fragility index using varied heating and cooling rates through a method described by Zheng et al.[39] The temperature profile used is described in Table S1. The $T_g$ determined through this method after cooling at 20°C/min and heating at 20°C/min is taken as the $T_g$ of a glass.

## 2.3 | Fragility index

Glass processing is determined largely by the viscosity behavior above the glass transition temperature, and as such, the kinetic fragility can be an important value to understand the viscosity behavior of a glass forming liquid.[40,41] The value of the calorimetric fragility index can be determined through $T_g$ measurements at varied heating rates through Equation (1) as follows:

$$\log\left(\frac{q_c}{q_{c,s}}\right) = m_{cal} - m_{cal}\frac{T_f^s}{T_f} \quad (1)$$

where $q_c$ is the DSC scan rate, $q_{c,s}$ is the standard DSC scan rate (typically 10°C/min), $m_{cal}$ is the calorimetric fragility index, $T_f^s$ is the fictive temperature at the standard scan rate, and $T_f$ is the fictive temperature at the specified scanning rate.[42] The calorimetric fragility index can be determined by taking the slope of the graph of $\log(1/q_c)$ versus $T_g/T_f$ . When the prior cooling rate is equal to the reheating rate, the difference between the onset of $T_g$ and the $T_f$ is minimal, and as such, the onset of $T_g$ can directly replace the $T_f$ to determine the slope of curve, and thus $m_{DSC}$.[43] The calorimetric fragility index is converted to a kinetic (viscosity) fragility index through the relationship by Zheng et al.[39]:

$$m_{vis} = 1.289(m_{cal} - m_0) + m_0 \quad (2)$$

where $m_{vis}$ is the kinetic viscosity fragility index and $m_0$ is 14.97. This kinetic viscosity fragility index can then be used to estimate the viscosity behavior of a liquid through the Mauro–Yue–Ellison–Gupta–Allan model.[40]

## 2.4 | Sulfur dilution

To quantify the concentration of polysulfides present in each glass, a sample was chosen that exhibited no $P^{1P}$ peak at 390 $cm^{-1}$ and a low concentration of polysulfides (sample 8, see Table S2). Known concentrations of additional sulfur were doped into sample 8 to quantify the amount of sulfur present from Raman peak analysis. Sample 8 was milled in the Spex 8000 M Mixer/Mill at 1725 rpm for 3 min to obtain a powdered form of the glass. Known amounts of additional sulfur were then added to this powder and then the Raman spectra were collected to create a composition plot of the intensity of the polysulfide peak at 473 $cm^{-1}$. For the concentration study, 0.2 g of glass powder was massed out along with an amount of sulfur to achieve concentrations ranging from 0.64 to 3.99 wt%, a range experimentally observed to span the range of Raman peak intensities at 473 $cm^{-1}$ of the as-prepared glasses. The sulfur and glass mixture was milled using a mortar and pestle for approximately 15 min per sample. Each sample was then packed into a die and pressed into a pellet at 1 metric ton force. Two pellets were pressed and tested for each dilution percentage.

## 2.5 | Raman spectroscopy

Bulk pieces of glass and pressed glass powder pellets were packed into a hermetically sealed Raman sample holder consisting of a recessed rectangular pocket deep enough to hold the samples and then covered with an ordinary glass slide sealed around the edges with vacuum grease. Raman spectra were collected using an InVia 488 nm Renishaw Coherent Laser Raman Micro-Spectrometer, calibrated to an internal standard silicon reference centered at 520.5 ± 0.4 $cm^{-1}$. The various samples were measured under a 20× objective lens, spot size ≈ $(50\,\mu m)^2$, at 12.5 mW power. Spectra were collected from 100 $cm^{-1}$ to 2000 $cm^{-1}$ using at least five accumulations.

The pressed powders were measured in essentially the same way. The samples were packed into the same hermetically sealed Raman sample holder and the spectra were collected using the same spectrometer as described above. Samples were tested using a 5× objective lens with a much larger spot size of approximately 500 $\mu m^2$ at 12.5 mW power. Each sample was tested in at least five different locations, and the spectra were added together to generate an average spectrum. The combination of using a larger sampling area and averaging the spectra from different areas was used to minimize the possible inhomogeneities in the sulfur distribution within the pressed pellet. Spectra were collected from 100 $cm^{-1}$ to 1000 $cm^{-1}$ with at least 10 accumulations.

# 3 | RESULTS

## 3.1 | Differential scanning calorimetry

A DSC thermogram for the 20°C/min scan is shown in Figure 1. The glass transition temperature ($T_g$) and

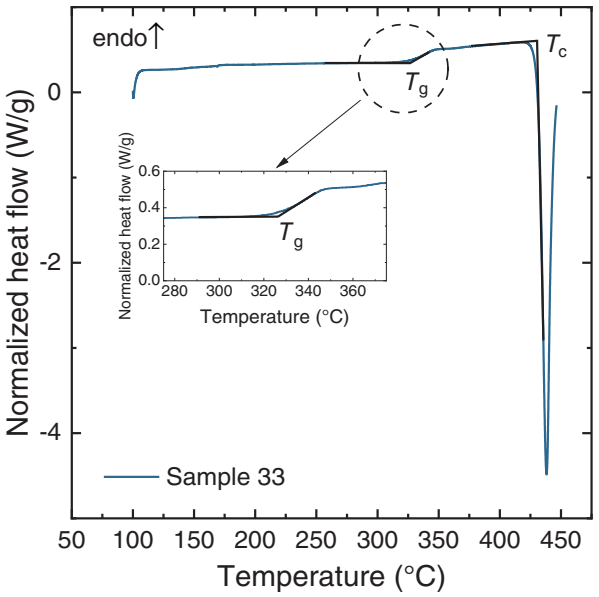


**FIGURE 1** Differential scanning calorimetry (DSC) thermogram (endothermic up) at 20°C/min heating rate showing the heating curve for sample 33 with the $T_g$ and $T_c$ marked.

crystallization temperature ($T_c$) are shown with values for both determined through the onset method. $T_g$ for the survey scan ranged from 308.3 to 328.5°C over the 33 samples of the same composition. The $T_g$ determined in the same way with the known cooling and heating rate of 20°C/min, $T_{g,20°C/min}$, varied from 304.3 to 330.7°C over the same 33 samples of the same composition. The $T_c$ ranged from 414.5 to 438.1°C. The working range, $\Delta T = T_c - T_g$, ranged from 86.8 to 126.3°C. A histogram for each value can be seen in Figure 2A–D. The full data can be found in Table S2.

The calorimetric fragility index was determined as described, with an example of the DSC thermograms shown in Figure 3A. The $T_g$ was calculated using the onset method. The determination of the calorimetric fragility index is shown through the fitting of the slope of the plot in Figure 3B. The calorimetric fragility was converted to a kinetic fragility through Equation (2). The values for the kinetic fragility index ranged from 49.9 to 74.3.

## 3.2 | Raman spectroscopy

Raman spectra were collected for each glass composition and as expected, only minor, yet statistically significant differences between the glasses were observed. Fully analyzed Raman spectra for samples 3, 9, and 26 that contained impurities and sample 0 used for comparison with no impurities can be found in Figure S1. The annotated Raman spectra for the same samples can be found in Figure 4A, that highlight the Raman bands for the $P^{1P}$ and polysulfide impurities.

From previous research on this and related glasses, we and others have attributed the broad peak at 251 $cm^{-1}$ to the symmetric bending mode of the $PS_4^{3-}$ tetrahedra.[44] The shoulders to the main peak located at 386 and 391 $cm^{-1}$ are attributed to the symmetric stretching modes of the $(SiS_4)^{4-}$ structure and of the $(P_2S_6)^{4-}$ defect structure, or $P^{1P}$ structure, respectively.[35,45,46] The main peak in the spectra centered at 423 $cm^{-1}$ is attributed to the symmetric $A_1$ stretch of the $PS_4^{3-}$ tetrahedra.[36,47] An impurity structure is present in some of the samples at 473 $cm^{-1}$ and is attributed to the symmetric stretch of S–S bonds present in the form of $S_8$ chains, rings, and the various polysulfides $^{-}S\text{-}(S_n)\text{-}S^{-}$.[48–50] In other chalcogenide glasses, particularly with highly covalent structures, -S–S- chains can be found between networking units, such as in Ge–S–S–Ge bonds in $Na_2S–GeS_2$ glasses, however, no one has so far reported on these bridging -S–S- bonds in highly modified invert thiosilicophosphate glasses.[51,52] Therefore, the mode at 473 $cm^{-1}$ is attributed to the stretching mode of S–S bonds in $S_8$ chains, rings, and the various polysulfides $^{-}S\text{-}(S_n)\text{-}S^{-}$.

To better distinguish the differences between the reference glass and the other samples, the spectrum of sample 0 glass that contained no impurity bands is subtracted from the other spectra to show only the changes that are present, which is shown in Figure 4B. Sample 0 is a glass made previously, that showed neither the $P^{1P}$ defect structure at 390 $cm^{-1}$ nor the polysulfide peak at 473 $cm^{-1+}$. Sample 0 is not included in the table as it was not tested for thermal properties. It can be seen, for example, that sample 3 shows a substantial amount of the $P^{1P}$ unit, sample 9 shows a substantial amount of polysulfide impurities, and sample 26 shows minimal change from sample 0. Other samples showed similar spectra and are omitted for clarity.

## 3.3 | Sulfur dilution

To quantify the amount of polysulfide impurities that are present in these glasses, sample 8 was taken and milled into a powder and then doped with a known concentration of sulfur ranging from 0.64 to 3.99 wt%. The Raman spectra were taken and averaged over many sample locations for each doped sample. The Raman spectra are shown in Figure 5. As expected, the intensity of the Raman spectral peaks due to sulfur located at 219 and 471 $cm^{-1}$ increase with increasing additional sulfur doped into the sample 8 powder.[53] Likewise, a very minor peak at 247 $cm^{-1}$ also increases with added sulfur.[53] While either or both peaks at 219 and 471 $cm^{-1}$ could have been used for this study, we focused on the peak at 471 $cm^{-1}$ because it appears to be the most intense in the glasses.

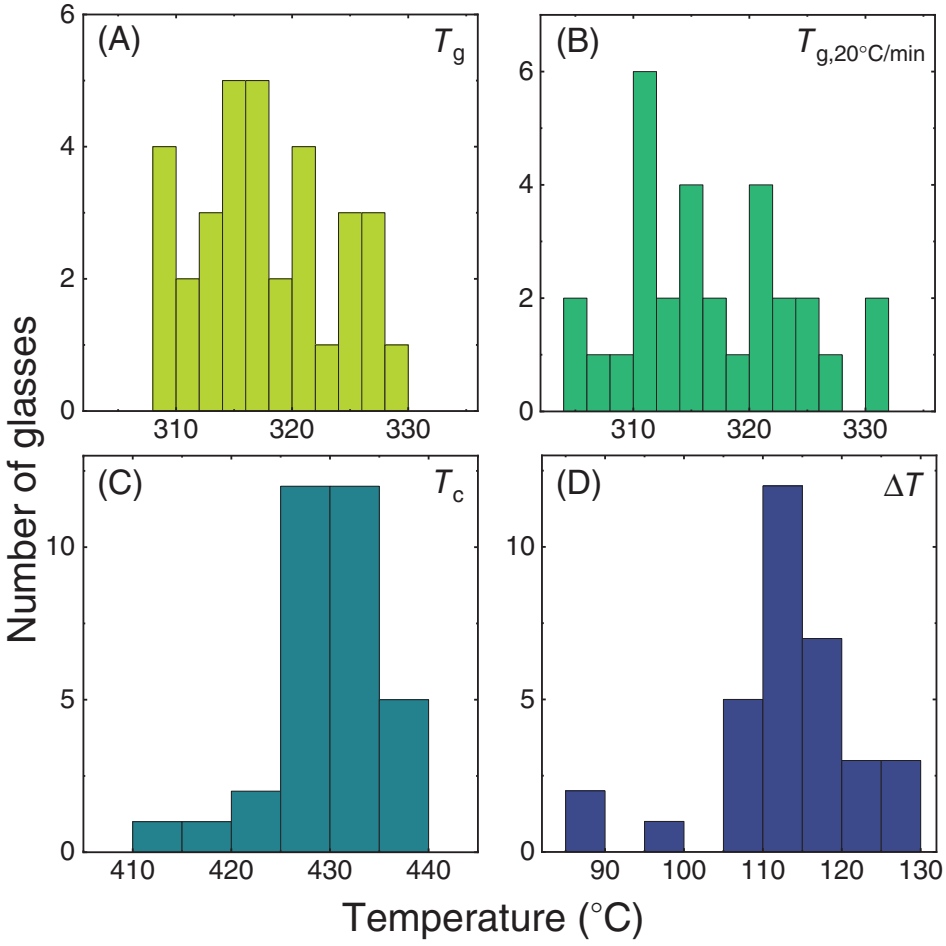


**FIGURE 2** Histograms showing distribution of thermal properties for (A) $T_g$, (B) $T_g$ at 20°C/min cooling/heating rate, (C) $T_c$, and (D) working range ($\Delta T$).

## 4 | DISCUSSION

### 4.1 | Raman peak analysis

The subtracted spectra shown in Figure 4B are analyzed to determine the size of each peak for each glass. Examples of the peak analysis for sample 9, which contains polysulfide impurities, and sample 3 which contains the $P^{1P}$ defect structure are shown in Figure 6A,B, respectively. The peak area was chosen for the analysis of the sulfur peak due to line broadening present compared to the sulfur doped samples. The peak height was chosen for analysis of the $P^{1P}$ as there is no simple way of doping in extra $P^{1P}$ units to the glass to determine its concentration as was done for polysulfide. The peak height relative to the $PS_4^{3-}$ mode is a simple method of determining the relative $P^{1P}$ concentration. The peak area for polysulfide containing glasses ranged from 0 to 4.3. The peak height for the $P^{1P}$ containing glasses varied from 0 to .14. It is interesting to note that no samples contain both the $P^{1P}$ and polysulfide impurities, suggesting that the sulfur atom given up in forming the $P^{1P}$ defect structure leaves the system, perhaps through volatilization, rather than becoming an impurity itself, leading to a sulfur deficiency.

### 4.2 | Quantification of polysulfide content

The Raman spectrum of sample 8 that had very minimal polysulfide and hence a very low intensity peak at 473 $cm^{-1}$ is subtracted from each of the other spectra of Figure 5 to subtract out the effect of the minor polysulfide content on the Raman spectra. This allowed a fit to be made to only the signal from the known addition of doped sulfur. These spectra are shown in Figure S2, and show the expected sulfur peaks in increasing peak area due to the increasing amount of added sulfur.[53] The peak located at 473 $cm^{-1}$ was chosen to be analyzed through peak fitting due to it being situated outside of most other peaks present in the spectra. Each peak was fitted, and the peak area was plotted against the amount of added sulfur, and this is shown

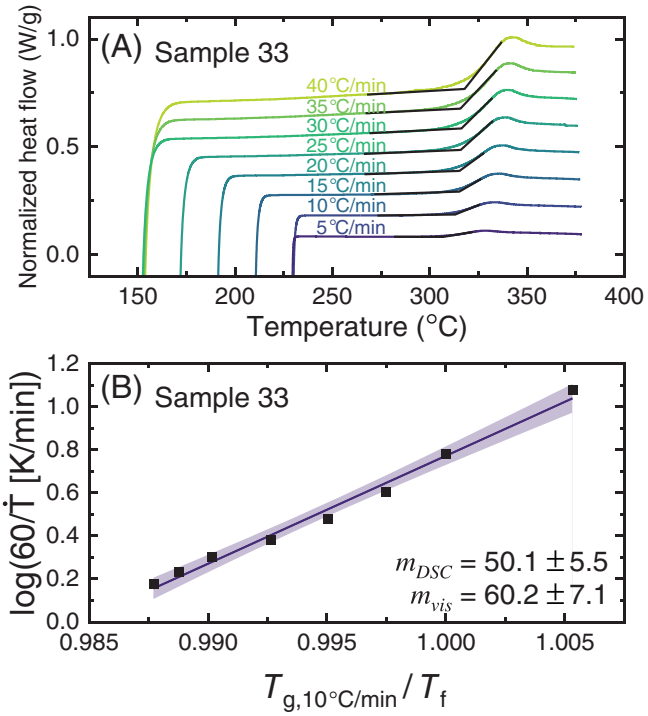


**FIGURE 3** (A) Differential scanning calorimetry (DSC) thermograms of sample 33 showing the fragility scan where the $T_g$ is determined at different paired heating and cooling rates. (B) The fitted line is used to determine the calorimetric fragility index. The shaded region indicates a 95% confidence interval for the slope and intercept of the line.

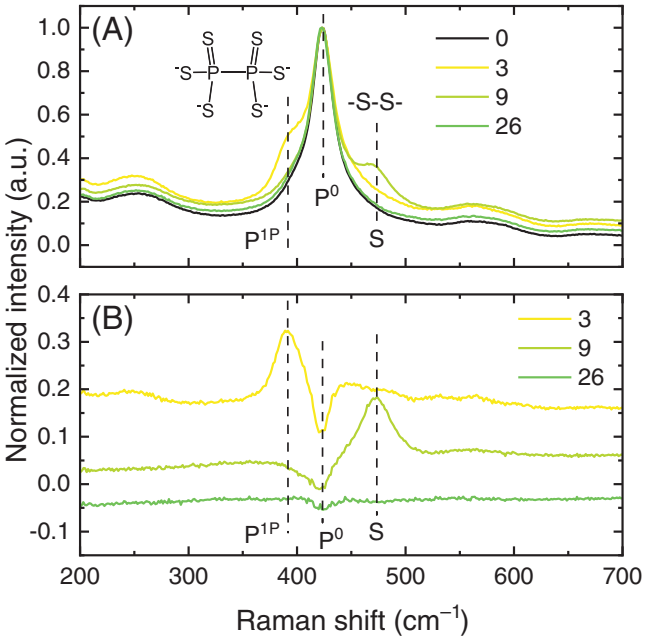


**FIGURE 4** (A) Raman spectra of sample 0 which contains no $P^{1P}$ nor polysulfide impurities, sample 3 which contains the $P^{1P}$ defect structure, sample 9 which contains polysulfide impurities, and sample 26 which matches well with the spectrum of sample 0. (B) Subtracted spectra showing changes from the reference sample for the same three samples. Fully annotated Raman spectra are given in Figure S1.

in Figure 7. The peak area was fit to the amount of added sulfur concentration and this is described by Equation (3) as follows:

$$C = \frac{A}{274.15} \tag{3}$$

where $A$ is the peak area, and $C$ is the sulfur concentration in wt%. The intercept in this linear expression is zero since the minor peak at 473 cm$^{-1}$ was subtracted from of the other spectra. Through this relationship, the peak area of the -S-S- peak at 473 cm$^{-1}$ in the Raman spectra for each glass can be converted to a concentration. In this way, it was found that the polysulfide concentration in all of the samples studied here ranged from 0 to 1.6 wt% sulfur.

## 4.3 | Multiple regression of structural impurities on thermal properties

To investigate the significance of the $P^{1P}$ defect structure and the polysulfide impurity on the thermal properties, a multiple regression model was developed and is given in

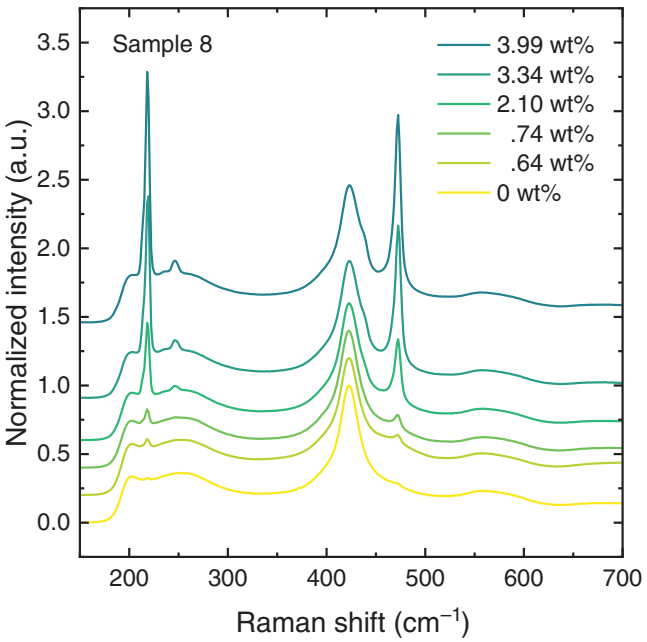


**FIGURE 5** Raman spectra for powder samples of sample 8 mixed with varying levels of added sulfur and pressed to s solid pellet for testing. Spectra were all normalized so that the height of the $PS_4^{3-}$ peak is equal to unity.

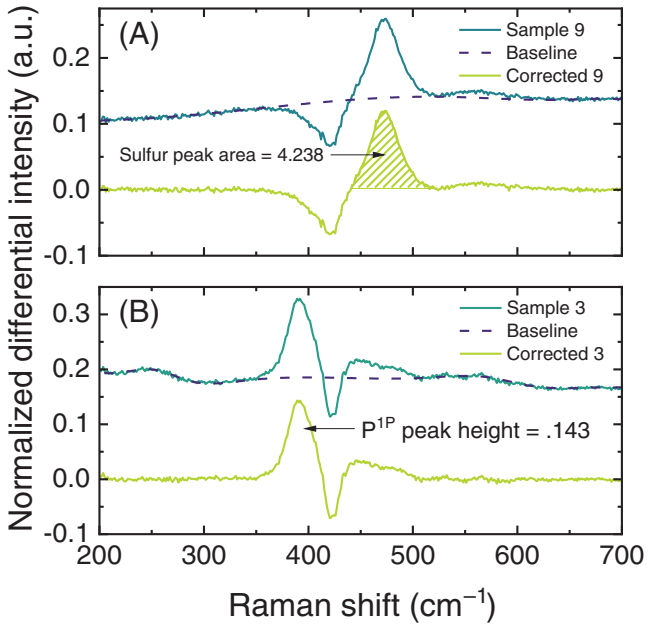


**FIGURE 6** (A) Analyzed differenatial Raman spectrum for sample 9, showing the peak area for the polysulfide impurity. (B) Analyzed differential Raman spectrum for sample 3, showing the peak height for the $P^{1P}$ defect structure.

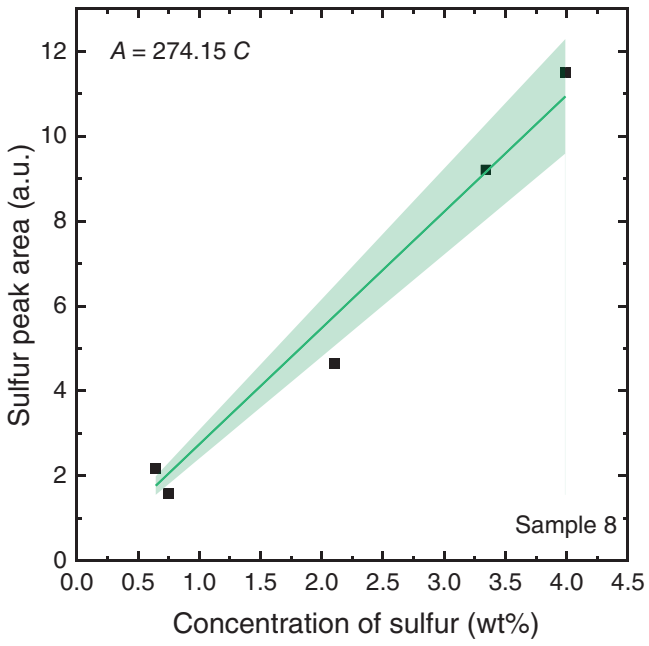


**FIGURE 7** Area of the sulfur peak located at 473 $cm^{-1}$ in the Raman spectra compared to the concentration of sulfur after subtracting out the spectrum of sample 8 that contained minimal polysulfide impurities. The linear fit assumed an intercept of 0 and the shaded region corresponds to a confidence interval of 95% for the slope of the line.

**TABLE 1** Values for the variables for the main effects and the interactions of each of the response variables ($T_g$, $T_c$, $\Delta T$, and $m_{vis}$) for the regression.

| Response | $\beta_0$ | SE | $\beta_1$ | SE | $\beta_2$ | SE | $\beta_{12}$ | SE |
|---|---|---|---|---|---|---|---|---|
| $T_g$ | 326 | 2.8 | 38 | 29 | -2.2 | 3.0 | -49 | 29 |
| $T_c$ | 412 | 4.1 | 85 | 42 | 20 | 4.4 | -88 | 43 |
| $\Delta T$ | 87 | 85 | 48 | 873 | 33 | 91 | -25 | 874 |
| $m_{vis}$ | 59 | 6.2 | -5.5 | 63 | 1.8 | 6.6 | 7.2 | 63 |

*Note*: Shaded cells indicate the following, green: $p$-value <.05, yellow: $p$-value <.10, and red: $p$-value >.10. SE is the standard error of each estimator from the linear regression.

Equation (4) as follows:

$$Y = \beta_0 + \beta_1 X_1 + \beta_2 X_2 + \beta_{12} X_1 X_2 + \varepsilon \quad (4)$$

where $Y$ is the response variable ($T_g$, $T_c$, $\Delta T$, or $m_{vis}$), $\beta_0$ is the estimated intercept of the regression model, $\beta_1$ is the estimated effect of the concentration, $X_1$ is the concentration covariate, $\beta_2$ is the estimated effect of the type of structural defect, $X_2$ is a categorical covariate describing the type of defect ($X_2 = 0$, if it is $P^{1P}$ and $X_2 = 1$, if it is polysulfide), $\beta_{12}$ is the estimated effect of the interaction effect between the type and the concentration, and $\varepsilon$ is the error. These parameters were estimated through multiple linear regression performed in the statistical software package R, with the code and outputs available in the Supporting Information. The models for each response variable are convoluted, and while they are a very effective statistical model for each data set, interpretation is challenging due to interaction effects between the different explanatory variables.

A graphical form of the model for each response variable is shown in Figures 8A–D. The model shows the fit to the change in the response variable with both the $P^{1P}$ and the polysulfide concentrations. The values for the regression parameters and their corresponding $p$-values are given in Table 1. From the regression models shown, it is seen that the $T_g$, $T_c$, and $\Delta T$ have a strong dependence on the type of defect, the concentration, and the interaction between the two. As the sample size of the $P^{1P}$ is small ($n = 3$), the $p$-values for the estimated covariates are high and may, therefore, not be statistically significant. A larger sample size for the $P^{1P}$ containing glasses would lead to more statistically significant values. However, the presence of these defects is detrimental to other glass properties, so the lack of many samples with the $P^{1P}$ defect speaks to the quality of the glass samples that were prepared. The model for the fragility index shows a slope that is very close to zero, and as such this model suggests that the fragility index is not closely correlated with the concentration of either the $P^{1P}$ defect structure or polysulfide impurities.

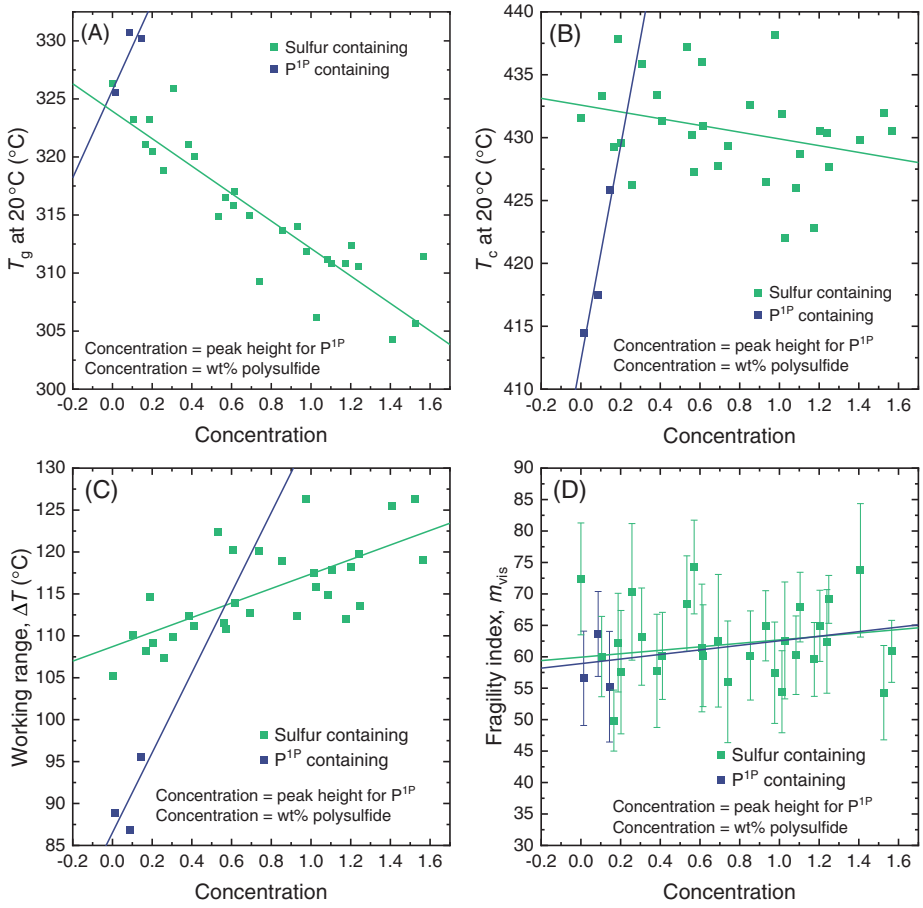


**FIGURE 8** Plots of each response variable ($T_g$, $T_c$, $\Delta T$, and $m_{vis}$) along with the corresponding linear regression for each situation. The regression line is extended for each plot to better show differences between the $P^{1P}$ and polysulfide impurities.

To better interpret the way in which polysulfide impurities and the $P^{1P}$ defect structure affect the values of these thermal properties, two other regression models were investigated. Here, the dataset was split into those that contain no $P^{1P}$ structural defect and those that contain no polysulfide. Sample 26 is included twice, one each in both datasets, as it, like sample 0, contained neither the $P^{1P}$ nor polysulfide impurities.

## 4.4 | Linear regression for polysulfide containing samples

A simple linear regression model was chosen to analyze the dependence of the thermal properties on the concentration of polysulfide impurities. The model is given in Equation (5) as follows:

$$Y = \beta_0 + \beta_1 X_1 + \varepsilon \tag{5}$$

where $Y$ is the response variable ($T_g$, $T_c$, $\Delta T$, or $m_{vis}$), $\beta_0$ is the estimate of the response variable at zero concentration, $\beta_1$ is the estimated expected change in the response variable per unit increase in the concentration, and $X_1$ is the concentration of either $P^{1P}$ or polysulfide impurities. The linear regressions for the thermal properties as a function of sulfur concentration can be seen in Figures 9A–D. The regression variables along with the $p$-values are given in Table 2. The $T_g$ of a sample appears to be very dependent on the concentration of polysulfide impurities. The estimate of the $T_g$ for a glass containing no polysulfide

**TABLE 2** Values for the regression variables for all response variables for both the polysulfide concentration and the concentration of $P^{1P}$ defect structure.

| | Polysulfide | | | | $P^{1P}$ | | | |
|---|---|---|---|---|---|---|---|---|
| Response | $\beta_0$ | SE | $\beta_1$ | SE | $\beta_0$ | SE | $\beta_1$ | SE |
| $T_g$ | 324 | .99 | -12 | 1.1 | 326 | 1.1 | 35 | 13 |
| $T_c$ | 433 | 1.4 | -2.7 | 1.6 | 423 | 7.0 | -2.5 | 82 |
| $\Delta T$ | 118 | 29 | 25 | 33 | 96 | 7.1 | -38 | 84 |
| $m_{vis}$ | 62 | 2.2 | .15 | 2.5 | 66 | 5.8 | -68 | 68 |

*Note*: Shaded cells indicate the following, green: $p$-value <.05, yellow: .05 ≤ $p$-value <.10, red: $p$-value >.10. SE is the standard error for each estimator.

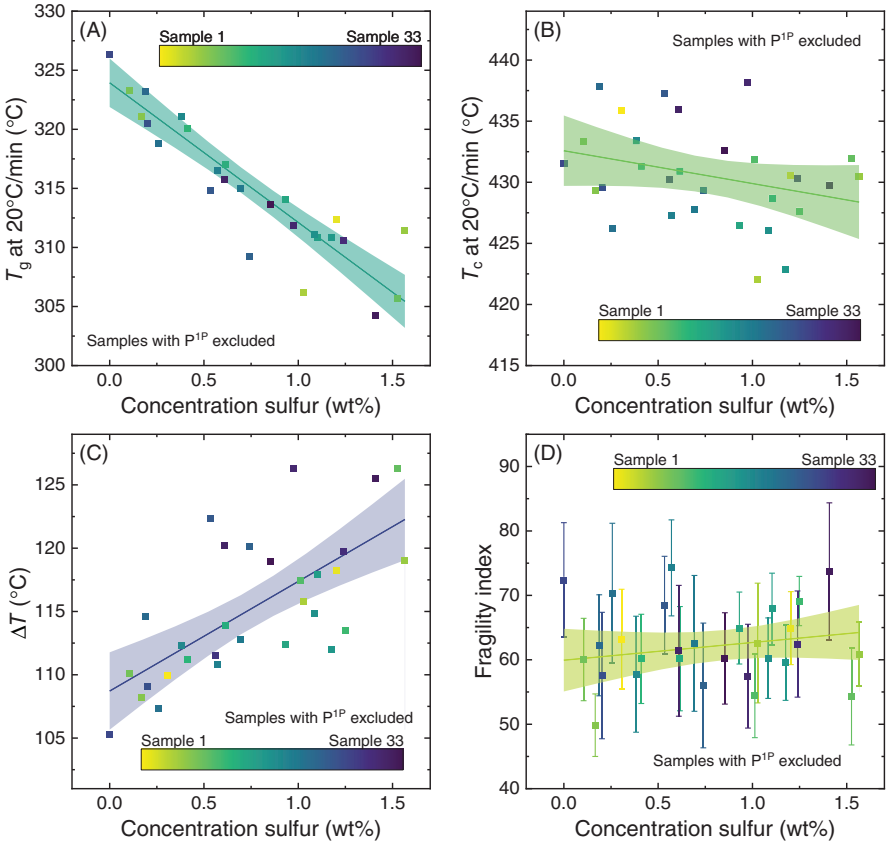


**FIGURE 9** (A) Plots of the linear regression for (A) $T_g$, (B) $T_c$, (C) $\Delta T$, and (D) $m_{vis}$ as a function of polysulfide concentration. Shaded regions indicate a 95% confidence interval for the regression.

impurities is 323.9 ± 1.9°C and for every 1 wt% sulfur added into the glass, the $T_g$ decreases by 11.7 ± 2.2°C. The relationship between $T_c$ and the polysulfide concentration is not statistically significant ($\alpha = .05$), and as such the relationship between $\Delta T$ and polysulfide concentration is also not statistically significant ($\alpha = .05$). However, it appears that higher concentrations of polysulfide impurities lower the $T_c$ slightly, while the substantial decrease in $T_g$ leads to a slightly larger working range. Such behavior is only conjecture at this point and is not conclusive and for this reason warrants further study. Similarly, the fragility index does not show a statistically significant relationship with the polysulfide concentration. Thus, from this data, it is suggested that polysulfides have a plasticizing effect on the glass transition temperature, lowering $T_g$ with increasing polysulfide content, but does not significantly alter the other thermal properties tested here.

## 4.5 | Linear regression for $P^{1P}$ containing samples

The same linear regression model described in Equation (5) was used to model the impact of the $P^{1P}$ defect structure on the same thermal properties. Plots of the linear regressions can be found in Figure 10A–D and the values of the regression variables can be found in Table 2. Due to the small sample size that contains the $P^{1P}$ defect structure, no statistically significant correlations were found between the height of the $P^{1P}$ peak and the thermal properties of this glass. However, from the estimates given, it appears that the $P^{1P}$ may have a substantial impact on the crystallization behavior of these glasses due to the 10°C decrease in the intercept ($\beta_0$) for the $T_c$ and a more than 20°C decrease in the intercept for the working range between the polysulfide containing glasses and the $P^{1P}$ containing glasses. While the small sample size makes it challenging to draw meaningful conclusions, this comparison suggests that the $P^{1P}$ does have an impact on the crystallization properties of these glasses and warrants further investigation.

## 5 | CONCLUSION

Evidence for polysulfide impurities and $P^{1P}$ defect structures was found in the Raman spectra of $Li_2S + SiS_2 + LiPO_3$ glasses. From the 33 samples

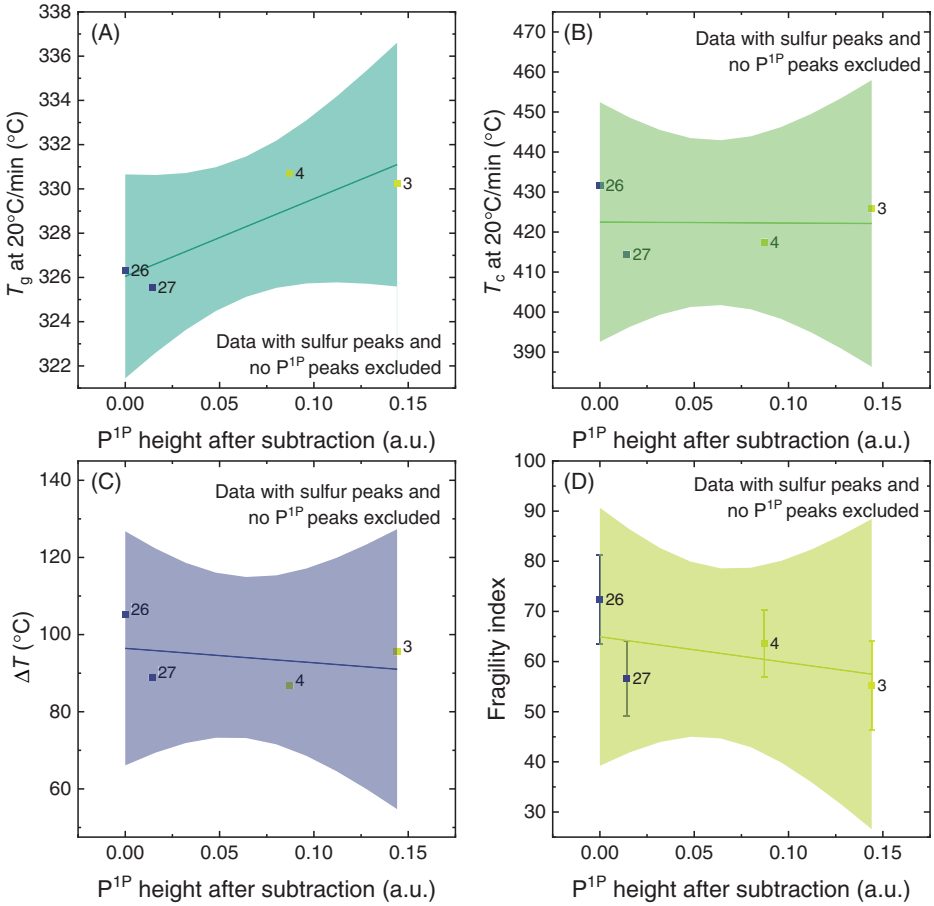


**FIGURE 10** (A) Plots of the linear regression for (A) $T_g$, (B) $T_c$, (C) $\Delta T$, and (D) $m_{vis}$ as a function of height of the $P^{1P}$ peak. Shaded regions indicate a 95% confidence interval for the regression.

synthesized, the concentration of polysulfide impurities was determined for each glass through the addition of known quantities of sulfur. The $T_g$, $T_c$, $\Delta T$, and $m_{vis}$ were measured and calculated for all of these glasses and were tested through three statistical models to determine the effects of polysulfide impurities and the $P^{1P}$ defect structure on each thermal property. Increasing sulfur impurity concentration leads to a lower $T_g$ but does not seem to significantly alter the other thermal properties. The $P^{1P}$ defect structure does not have a statistically significant impact on the thermal properties measured, however this is largely due to the small sample size ($n = 3$). The data suggests that the $P^{1P}$ defect structure affects the crystallization behavior of the glass, reducing its resistance to crystallization. Further research is necessary to more fully understand the impact of the $P^{1P}$ defect structure on the thermal and other properties of these glasses.

## AUTHOR CONTRIBUTIONS

The manuscript was written through contributions of all authors. All authors have given approval to the final version of the manuscript.

## ACKNOWLEDGMENTS

The authors would like to thank other members of the Glass and Energy Materials Group at Iowa State for help in synthesizing the glasses, particularly Victor M. Torres III and Jordan Ryner, and the Statistical Consulting Group at Iowa State for their help in analyzing the data and developing the interaction model, particularly Eryn Blagg.

Open access funding provided by the Iowa State University Library.

## ORCID

*Jacob Wheaton* https://orcid.org/0000-0001-8461-9393
*Steve W. Martin* https://orcid.org/0000-0002-6472-509X

## REFERENCES

1. Masias A, Marcicki J, Paxton WA. Opportunities and challenges of lithium ion batteries in automotive applications. ACS Energy Lett. 2021;6(2):621–30.
2. Sun Y-K. Promising all-solid-state batteries for future electric vehicles. ACS Energy Lett. 2020;5(10):3221–23.
3. Levy SC. Safety and reliability considerations for lithium batteries. J Power Sources. 1997;68(1):75–77.

4. Chen Y, Kang Y, Zhao Y, Wang L, Liu J, Li Y, et al. A review of lithium-ion battery safety concerns: the issues, strategies, and testing standards. J Energy Chem. 2021;59:83–99.
5. Famprikis T, Canepa P, Dawson JA, Islam MS, Masquelier C. Fundamentals of inorganic solid-state electrolytes for batteries. Nat Mater. 2019;18(12):1278–91.
6. Zhao Q, Stalin S, Zhao C-Z, Archer LA. Designing solid-state electrolytes for safe, energy-dense batteries. Nat Rev Mater. 2020;5(3):229–52.
7. Manthiram A, Yu X, Wang S. Lithium battery chemistries enabled by solid-state electrolytes. Nat Rev Mater. 2017;2(4):16103.
8. Yu T, Yang X, Yang R, Bai X, Xu G, Zhao S, et al. Progress and perspectives on typical inorganic solid-state electrolytes. J Alloys Compd. 2021;885:161013.
9. Zhao W, Yi J, He P, Zhou H. Solid-state electrolytes for lithium-ion batteries: fundamentals, challenges and perspectives. Electrochem Energy Rev. 2019;2(4):574–605.
10. Wang Y, Song S, Xu C, Hu N, Molenda J, Lu L. Development of solid-state electrolytes for sodium-ion battery–a short review. Nano Mater Sci. 2019;1(2):91–100.
11. Wu C-W, Ren X, Zhou W-X, Xie G, Zhang G. Thermal stability and thermal conductivity of solid electrolytes. APL Mater. 2022;10(4):040902.
12. Chen R, Qu W, Guo X, Li L, Wu F. The pursuit of solid-state electrolytes for lithium batteries: from comprehensive insight to emerging horizons. Mater Horiz. 2016;3(6):487–516.
13. Gao Z, Sun H, Fu L, Ye F, Zhang Y, Luo W, et al. Promises, challenges, and recent progress of inorganic solid-state electrolytes for all-solid-state lithium batteries. Adv Mater. 2018;30(17):1705702.
14. Han F, Westover AS, Yue J, Fan X, Wang F, Chi M, et al. High electronic conductivity as the origin of lithium dendrite formation within solid electrolytes. Nat Energy. 2019;4(3):187–96.
15. Kazyak E, Chen K-H, Wood KN, Davis AL, Thompson T, Bielinski AR, et al. Atomic layer deposition of the solid electrolyte garnet $Li_7La_3Zr_2O_{12}$. Chem Mater. 2017;29(8):3785–92.
16. Buschmann H, Doelle J, Berendts S, Kuhn A, Bottke P, Wilkening M, et al. Structure and dynamics of the fast lithium ion conductor "$Li_7La_3Zr_2O_{12}$". Phys Chem Chem Phys. 2011;13(43):19378–92.
17. Chen RJ, Liang W, Zhang HQ, Wu F, Li L. Preparation and performance of novel LLTO thin film electrolytes for thin film lithium batteries. Chin Sci Bull. 2012;57(32):4199–204.
18. Li CL, Zhang B, Fu ZW. Physical and electrochemical characterization of amorphous lithium lanthanum titanate solid electrolyte thin film fabricated by e-beam evaporation. Thin Solid Films. 2006;515(4):1886–92.
19. Ahn J-K, Yoon S-G. Characteristics of amorphous lithium lanthanum titanate electrolyte thin films grown by PLD for use in rechargeable lithium microbatteries. Electrochem Solid-State Lett. 2005;8(2):A75–A78.
20. Ahn J-K, Yoon S-G. Characteristics of perovskite $(Li_{0.5}La_{0.5})TiO_3$ solid electrolyte thin films grown by pulsed laser deposition for rechargeable lithium microbattery. Electrochim Acta. 2004;50(2–3):371–74.
21. Zhang Q, Cao D, Ma Y, Natan A, Aurora P, Zhu H. Sulfide-based solid-state electrolytes: synthesis, stability, and potential for all-solid-state batteries. Adv Mater. 2019;31(44):1901131.
22. Wang C, Fu K, Kammampata SP, McOwen DW, Samson AJ, Zhang L, et al. Garnet-type solid-state electrolytes: materials, interfaces, and batteries. Chem Rev. 2020;120(10):4257–300.
23. Cao C, Li Z-B, Wang X-L, Zhao X-B, Han W-Q. Recent advances in inorganic solid electrolytes for lithium batteries. Front Energy Res. 2014;2:1–10.
24. Liang F, Sun Y, Yuan Y, Huang J, Hou M, Lu J. Designing inorganic electrolytes for solid-state Li-ion batteries: a perspective of LGPS and garnet. Mater Today. 2021;50:418–41.
25. Kennedy JH, Zhang Z, Eckert H. Ionically conductive sulfide-based lithium glasses. J NonCryst Solids. 1990;123(1):328–38.
26. Chandra A, Bhatt A, Chandra A. Ion conduction in superionic glassy electrolytes: an overview. J Mater Sci. 2013;29(3):193–208.
27. Tatsumisago M. Glassy materials based on $Li_2S$ for all-solid-state lithium secondary batteries. Solid State Ionics. 2004;175(1):13–18.
28. Yersak T, Salvador JR, Schmidt RD, Cai M. Hybrid Li-S pouch cell with a reinforced sulfide glass solid-state electrolyte film separator. Int J Appl Glass Sci. 2021;12(1):124–34.
29. Garcia-Mendez R, Mizuno F, Zhang R, Arthur TS, Sakamoto J. Effect of processing conditions of $75Li_2S$-25P2S5 solid electrolyte on its DC electrochemical behavior. Electrochim Acta. 2017;237:144–51.
30. Kmiec S, Olson M, Kenney M, Martin SW. Interpretation of the Na+ ionic conductivity in $Na_4P_2S_{7-x}O_x$ mixed oxy-sulfide glasses: effects of oxygen doping. Chem Mater. 2022;34(21):9479–91.
31. Zhao R, Hu G, Kmiec S, Wheaton J, Torres Iii VM, Martin SW. Grain-boundary-free glassy solid electrolytes based on sulfide materials: effects of oxygen and nitrogen doping on electrochemical performance. Batter Supercaps. 2022;5(11):e202100356.
32. Tatsumisago M, Hayashi A. Superionic glasses and glass–ceramics in the $Li_2S$–$P_2S_5$ system for all-solid-state lithium secondary batteries. Solid State Ion. 2012;225:342–45.
33. Zhao R, Hu G, Kmiec S, Gebhardt R, Whale A, Wheaton J, et al. New amorphous oxy-sulfide solid electrolyte material: anion exchange, electrochemical properties, and lithium dendrite suppression via in situ interfacial modification. ACS Appl Mater Interfaces. 2021;13(23):26841–52.
34. Dietrich C, Weber DA, Sedlmaier SJ, Indris S, Culver S P, Walter D, et al. Lithium ion conductivity in $Li_2S$–$P_2S_5$ glasses–building units and local structure evolution during the crystallization of superionic conductors $Li_3PS_4$, $Li_7P_3S_{11}$ and $Li_4P_2S_7$. J Mater Chem A. 2017;5(34):18111–19.
35. Olson M, Kmiec S, Martin SW. NaPON doping of $Na_4P_2S_7$ glass and its effects on the structure and properties of mixed oxy-sulfide-nitride phosphate glass. Inorg Chem. 2022;61(44):17469–84.
36. Kmiec S, Joyce A, Martin SW. Glass formation and structural analysis of $Na_4P_2S_7$-xOx, $0 \leq x \leq 7$ sodium oxy-thiophosphate glasses. J NonCryst Solids. 2018;498:177–89.
37. Watson DE, Martin SW. Structural characterization of the short-range order in high alkali content sodium thiosilicophosphate glasses. Inorg Chem. 2018;57(1):72–81.
38. Wheaton J, Kmiec S, Schuler D, Sorensen C, Martin S W. Electrochemical behavior of drawn thin-film vitreous lithium metaphosphate. ACS Appl Energy Mater. 2021;4(10):10835–42.
39. Zheng Q, Mauro JC, Yue Y. Reconciling calorimetric and kinetic fragilities of glass-forming liquids. J NonCryst Solids. 2017;456:95–100.

40. Mauro JC, Yue Y, Ellison AJ, Gupta P, Allan DC. Viscosity of glass-forming liquids. Proc Natl Acad Sci. 2009;106(47):19780–84.
41. Angell CA. Formation of glasses from liquids and biopolymers. Science. 1995;267(5206):1924–35.
42. Zheng Q, Zhang Y, Montazerian M, Gulbiten O, Mauro JC, Zanotto ED, Yue Y. Understanding glass through differential scanning calorimetry. Chem Rev. 2019;119(13):7848–939.
43. Yue Y, von der Ohe R, Jensen SL. Fictive temperature, cooling rate, and viscosity of glasses. J Chem Phys. 2004;120(17):8053–59.
44. Kim J, Yoon Y, Eom M, Shin D. Characterization of amorphous and crystalline $Li_2S$–$P_2S_5$–$P_2Se_5$ solid electrolytes for all-solid-state lithium ion batteries. Solid State Ion. 2012;225:626–30.
45. Ohara K, Mitsui A, Mori M, Onodera Y, Shiotani S, Koyama Y, et al. Structural and electronic features of binary $Li_2S$-$P_2S_5$ glasses. Sci Rep. 2016;6(1):21302.
46. Zhao R, Kmiec S, Hu G, Martin SW. Lithium thiosilicophosphate glassy solid electrolytes synthesized by high-energy ball-milling and melt-quenching: improved suppression of lithium dendrite growth by Si doping. ACS Appl Mater Interfaces. 2020;12(2):2327–37.
47. Noi K, Hayashi A, Tatsumisago M. Structure and properties of the $Na_2S$–$P_2S_5$ glasses and glass–ceramics prepared by mechanical milling. J Power Sources. 2014;269:260–65.
48. Bischoff C, Schuller K, Haynes M, Martin SW. Structural investigations of $yNa_2S+(1-y)PS_{5/2}$ glasses using Raman and infrared spectroscopies. J NonCryst. Solids. 2012;358(23):3216–22.
49. Andrikopoulos KS, Kalampounias AG, Falagara O, Yannopoulos SN. The glassy and supercooled state of elemental sulfur: vibrational modes, structure metastability, and polymer content. J Chem Phys. 2013;139(12):124501.
50. Ohtomo T, Mizuno F, Hayashi A, Tadanaga K, Tatsumisago M. Mechanochemical synthesis of lithium ion conducting glasses and glass–ceramics in the system $Li_2S$–P–S. Solid State Ion. 2005;176(31):2349–53.
51. Kassem M, Bounazef T, Sokolov A, Bokova M, Fontanari D, Hannon AC, et al. Deciphering fast ion transport in glasses: a case study of sodium and silver vitreous sulfides. Inorg Chem. 2022;61(32):12870–85.
52. Kmiec S, Joyce A, Bayko D, Martin SW. Glass formation and structure of melt quenched mixed oxy-sulfide $Na_4P_2S_{7-x}O_x$ glasses for $0 \leq x \leq 5$. J NonCryst Solids. 2020;534:119776.
53. Ward AT. Raman spectroscopy of sulfur, sulfur-selenium, and sulfur-arsenic mixtures. J Phys Chem. 1968;72(12):4133–39.

## SUPPORTING INFORMATION

Additional supporting information can be found online in the Supporting Information section at the end of this article.

**How to cite this article:** Wheaton J, Martin SW. Impact of impurities on the thermal properties of a $Li_2S$–$SiS_2$–$LiPO_3$ glass. Int J Appl Glass Sci. 2024;1–12. https://doi.org/10.1111/ijag.16654